PROCEEDINGS, 51st Workshop on Geothermal Reservoir Engineering
Stanford University, Stanford, California, February 9-11, 2026
SGP-TR-230

Standardized Definitions and Permeability Regimes for the Characterization and Capacity Estimation of Geothermal Systems

Ryan B. Libbey and John F. Murphy

Ormat Technologies, Inc. 6884 Sierra Center Pkwy, NV, USA 89511

rlibbey@ormat.com

Keywords: Resource Geometry, Resource Capacity Estimations, Recovery Factors

ABSTRACT

Key geothermal resource parameters such as *Area*, *Thickness*, *Temperature*, and *Recovery Factor* play an important role in the characterization of resources, the identification of appropriate analogs, and the estimation of resource capacities. There are currently no industry-wide standards of these parameters in the context of geothermal resource assessments, resulting in inconsistent approaches to resource capacity estimations and confusion when communicating such parameters to both specialists and non-specialists alike. The definitions presented herein focus on a conceptual model approach to *Area* and a *Thickness* parameter rooted in the concept of heat-sweeping in a hypothetical or realized development. Supported by definitions and explanations of rules and exceptions for estimating *Area*, *Thickness* and *Temperature*, this study computes *Recovery Factors* for forty geothermal fields from a wide range of geologic settings. Additionally, an approach is presented to categorizing geothermal fields based on their *Permeability Regime*; a resource descriptor that is controlled by geologic setting and that influences parameters such as *Area*, well permeability, feedzone distributions, *Recovery Factors*, and post-development cooling trends. Four end-member *Permeability Regimes* are proposed to describe all naturally-occurring geothermal systems: Discrete, Limited Distributed, Enhanced Distributed, and Stratigraphic. The relationship of these permeability regimes to well productivity index values and *Recovery Factors* are described herein. This paper outlines an approach to standardize the documentation of key resource characteristics and *Permeability Regimes* for all geothermal systems, regardless of temperature or geologic setting. A companion paper reviewing the reservoir engineering characteristics of geothermal *Permeability Regimes* is provided by Murphy and Libbey (2026).

1. INTRODUCTION

1.1 The Need for Standardized Definitions

Key resource parameters such as *Area*, *Thickness*, and *Temperature* play an important role in the characterization of geothermal resources, the identification of appropriate analogs, and the calculation of resource capacity estimates. There are currently no industry-wide standard definitions of resource geometry (e.g., resource *Area* and *Thickness*), resulting in inconsistent approaches applied to resource capacity estimations and confusion when communicating such parameters to specialists and non-specialists alike. The methodology presented herein is an approach to geothermal resource parameter description that is conceptual model- as well as conceptual development-driven, and is designed to be appropriate across geological settings, *Permeability Regimes*, and resource temperature ranges. The conceptual development aspect of this approach refers to the consideration of whether a system is likely to be developed in the upflow, outflow, or both, as this is likely to impact the described *Area*, *Thickness*, *Temperature*, and *Permeability Regime* parameters as detailed further in the body of this text and illustrated in Figure 7.

1.2 Probabilistic Resource Capacity Assessments

A primary goal of the definitions and methodology detailed in this paper is to provide a framework for increasing the consistency of inputs into volumetric capacity estimation equations, and to consider the influence of permeability on the *Recovery Factors* utilized in these calculations. There will always be some degree of uncertainty regarding the geometry of a studied geothermal system, regardless of the project phase. Accordingly, probabilistic approaches that utilize lognormally distributed ranges for area, thickness, temperature, and *Recovery Factor* are recommended over deterministic inputs for these variables. Robust conceptual models and reviews of analog systems are essential for defining reasonable probabilistic ranges of the variables utilized in these capacity estimation equations. A recommended standardized approach to defining *Temperature*, *Thickness*, and *Area* is provided in this study, alongside recommendations for utilizing *Permeability Regimes* to refine the probabilistic ranges of *Recovery Factors* that are incorporated into volumetric heat-in-place resource capacity equations.

1.3 Calibration Analogs

Forty developed geothermal fields from a wide range of geologic settings have been characterized using the *Temperature*, *Area*, *Thickness*, and *Permeability Regime* definitions described herein (Table 1). For each of these *Calibration Analogs*, available time-series data of mass flow, enthalpy, and power generation alongside forecasts from numerical models have been utilized to estimate a *30-Year Average Power Capability* in MWe_{gross}, where MWe_{gross} refers to the theoretical electric power produced from a modern plant design but not accounting for the plant parasitic loads (condensers, cycle pumps, etc., generally 10-12%) nor accounting for any wellfield parasitics (production pumps, injection booster pumps, etc.) which will vary widely depending on resource conditions. *The 30-Year*

Average Power Capability is different than the listed installed MW capacity of a field and is also not necessarily equal to the reported generation values for some of the *Calibration Analogs* – as is the case in some fields with aging facilities, where contemporary plant designs could theoretically generate notably more power than is reported with the available flow rate and enthalpy data. *Recovery Factors* for these *Calibration Analogs* are then solved for using a volumetric heat-in-place equation, fixing the *30-Year Average Power Capability* value as the mean capacity estimate, defining start-up *Temperature* value, and utilizing probabilistic ranges for *Area* and *Thickness* following the proposed standards in this paper. Monte Carlo methods are then used to calculate the probabilistic distributions of power capacities, with conversion efficiencies of the volumetric heat-in-place equation consistent with modern geothermal power plant technologies and that are also a function of the injection temperature and average annual air temperature in the utilized equation.

Table 1. Summary table of *Calibration Analogs* utilized in this study.

Permeability Regime	Field Name	Abbr.	COD	Approx. Installed Capacity (2025)	Analog Score						Start-Up Temp	Area P90	Area Mean	Area P10	Area Slice Elev.	Thick. P90	Thick. Mean	Thick. P10	Recovery Factor	MPWPI
					Longevity	Operating Capacity	30yr Avg. MW Est.	Geometry Charac.	Perm. Charac.	Cal. Analog Tier										
				MWe							°C	km^2	km^2	km^2	mrsl	m	m	m		kg/s/bar
Discrete	Beowawe, USA	BE	1985	17.7	A	A	B	B	A	2	210	0.6	0.8	1	-760	990	1255	1550	0.240	33
	Blue Mountain, USA	BM	2009	49.5	B	A	B	A	A	2	190	1	1.2	1.5	-540	1900	2410	2970	0.165	11.7
	Brady, USA	BR	1992	24	A	A	A	A	A	1	182	0.8	1.1	1.5	+245	1210	1535	1890	0.265	17.5
	Dixie Meadows, USA	DM	---	---	D	-	D	B	A	4	152	0.5	0.7	1	0	1050	1330	1640	0.340	119
	Jersey Valley, USA	JV	2011	15	B	A	A	B	A	2	167	0.5	0.8	0.8	+40	1105	1400	1725	0.160	7.1
	McGinness Hills, USA	MH	2012	146	B	A	B	C	A	2	165	1.75	2.6	3.5	+760	1530	1940	2390	0.400	63
	Neal, USA	NE	2012	32	B	A	A	C	A	2	141	1	1.3	1.75	-740	1410	1790	2205	0.320	164.5
	Paisley, USA	PA	2014	3	B	A	D	D	C	4	115	0.7	0.9	1.25	+600	895	1135	1400	0.185	7.9
	Tungsten Mtn, USA	TM	2017	38	B	A	A	B	A	2	141	1	1.3	1.75	+480	1345	1710	2105	0.350	45.4
	Tuscarora, USA	TU	2012	18	B	A	A	A	A	1	174	1	1.2	1.5	+225	1130	1430	1765	0.210	7.9
Limited Distributed	Amatitlan, GTM○	AM	2007	20	A	A	B	C	A	2	275	1.75	2.5	3.25	+200	645	820	1010	0.064	0.5
	Desert Peak, USA	DP	1985	26	A	A	B	A	B	1	209	2	2.5	3	+275	1190	1505	1855	0.050	3.5
	The Geysers, USA	GE	1960	~900	A	A	A	C	C	3	240	80	101.5	110	-1300	2080	2640	3250	0.060	3
	Ijen, IDN	IJ	2025	34	D	B	B	B	A	3	285	1.25	1.5	1.75	-300	1630	2070	2545	0.094	0.6
	Kamojang, IDN	KA	1983	235	A	A	C	A	C	3	240	13	17.3	22	+165	1335	1695	2090	0.080	1.5
	Momotombo, NIC○	MO	1983	77	A	A	C	B	B	3	240	1.5	1.8	2.25	-1180	1260	1600	1975	0.135	1.7
	Mount Apo, PHL○	MA	1997	107	A	A	C	C	B	3	260	6	8.8	12	0	860	1090	1340	0.140	2
	Mutnovsky, RUS○	MU	1999	62	A	A	C	B	B	3	250	4	4.7	5.5	-250	1800	2285	2815	0.070	2.2
	Patua, USA	PT	2013	25.1	B	A	B	B	B	2	153	6.25	7.7	9.25	-1260	1580	2010	2475	0.040	3.3
	Raft River, USA	RR	2007	13	A	A	A	B	A	2	140	7	8.9	11	-200	830	1050	1295	0.039	1.9
	San Jacinto, NIC	SJ	2012	72	B	A	C	B	B	3	272	1.75	2.3	2.85	-1640	1470	1865	2295	0.154	2
	Soda Lake, USA	SL	1987	23	A	A	B	A	B	1	184	1.75	2.2	2.75	+50	1040	1320	1625	0.094	1.5
	Sumikawa, JPN	SU	1995	50	A	A	C	C	B	2	280	2.5	3	3.5	-570	1070	1355	1670	0.079	0.6
	Zunil, GTM	ZU	1999	20	A	A	B	C	A	2	275	0.75	1	1.25	+900	1025	1300	1600	0.130	1
Enhanced Distributed	Bouillante, FRA	BO	1986	15	A	C	B	C	A	3	251	0.75	1	1.4	-1060	1115	1415	1745	0.248	50
	Cove Fort, USA○	CF	2013	18	B	C	B	B	A	3	154	2	2.5	3	+1200	1150	1460	1800	0.490	152
	Dixie Valley, USA	DV	1988	64	A	B	A	B	B	2	242	2.75	3.8	5	-1700	1605	2040	2510	0.145	13.9
	Don A Campbell, USA●	DC	2013	28	B	A	B	B	A	2	128	3.5	4	4.5	+925	835	1060	1305	0.410	250
	Mokai, NZ	MK	1999	110	A	A	B	A	B	1	312	2	2.3	2.75	-1300	1200	1520	1875	0.210	5
	Ngā Tamariki, NZ	NT	2013	86	B	A	B	B	B	2	280	1.5	1.8	2.25	-1900	2400	3045	3750	0.187	13
	Olkaria West, KEN	OW	2000	150	A	A	B	B	A	1	275	7	8.2	9.5	+165	1210	1535	1890	0.095	8.3
	Reykjanes, ISL	RE	2006	100	A	A	C	A	A	1	290	2.5	2.7	3	-1875	1570	1995	2455	0.162	6
	Salak, IDN○	SA	1997	377	A	A	C	A	C	3	270	7	8.5	10	-790	1745	2215	2725	0.220	10
	Salt Wells, USA●	SW	2009	9	B	A	B	A	A	1	136	0.9	1.2	1.6	+1150	655	830	1020	0.530	163
	Steamboat, USA○	SB	1988	79	A	A	A	A	A	1	168	3	3.6	4.5	+1275	1045	1325	1635	0.450	141
	Tiwi, PHL○	TI	1979	234	A	A	B	A	C	2	275	6	7.3	8.75	-1065	915	1160	1430	0.180	7
Strat.	Bruchsal, DEU	BC	2009	0.55	B	-	A	-	A	4	126	2	2.4	2.75	-2200	150	195	250	0.050	0.6
	Ormesa, USA	OM	1986	36	A	A	A	A	A	1	151.6	10.5	11.7	13	-1220	1455	1845	2270	0.146	7
	Heber, USA	HE	1985	91	A	A	A	A	A	1	175	4	4.7	5.5	-1920	1810	2295	2825	0.232	8.4
	Salton Sea, USA	SS	1982	432	A	A	B	B	B	3	270*	30	37	45	-2070	2180	2765	3410	0.053	5

● = System dominantly producing from outflows, ○ = Systems notably producing from both outflow and upflow regions. Salinity-corrected liquid enthalpy values were utilized in the volumetric heat-in-place equation used to calculate the 30-Year Power Capability for the Salton Sea, resulting in an effective start-up resource temperature of 215°C compared to the average estimated formation temperature of ~270°C. The authors endeavored to accurately characterize the studied systems using the available data but acknowledge that many details of each system are approximate or may not accurately reflect the most up-to-date resource understanding. Support and corrections to improve this dataset are gladly welcomed.

A median production well productivity index (MPWPI) is also assembled for each field (further detailed by Murphy and Libbey, 2026) to assess the influence of well permeability on *Recovery Factors* for geothermal developments. The MPWPI is estimated from kh or well flow parameters for a minority of the non-Ormat *Calibration Analogs*, where productivity index (PI) data are not publicly available. A selection of the utilized *Calibration Analogs* and their defined parameters are provided in Table 1. These Calibration Analogs are categorized into four tiers based on their perceived reliability (1 = most reliable), which is a function of their scores (A to D) for: (1) longevity of operations, (2) the ratio of the operating capacity relative to the estimated *30-Year Average Power Capability*, (3) the confidence of the *30-Year Average Power Capability* estimate, (4) the degree of certainty regarding the isotherm geometry and *Thickness* of the system, and (5) the degree of certainty for the well permeability estimates of the field.

The process of creating the forty *Calibration Analogs* utilized in this study involved the assembly of P-T logs, reservoir time-series data, isotherm maps, wellfield/welltrace maps, geological/geophysical/geochemical data, conceptual model cross-sections, well permeability data, feedzone distributions, and numerical model information and forecasts from published literature alongside previously unpublished datasets for a few of the operating Ormat fields in this list. The resulting list of *Calibration Analogs* includes fields with a diverse range of geologic settings and resource temperatures; from >300°C systems in volcanic arcs to <130°C systems in sedimentary basins. Systems that produce dominantly from the upflow, outflow, or a combination of both, are represented in the dataset (Table 1), along with one developed system (Bruchsal) situated within a sedimentary basin with conductive thermal gradients.

Some specific references that were drawn on, listed in alphabetical order by field name include: **Amatitlan** (Menzies et al., 1996; Porras and Xicara, 2020), **Beowawe** (Layman, 1984; Wiggins et al., 2025), **Blue Mountain** (Melosh et al., 2008; Fercho et al., 2023), **Bouillante** (Lachassagne et al., 2009), **Brady** (Siler et al., 2021), **Bruchsal** (Herzberger et al., 2010; Meixner et al., 2016; Stober et al., 2017), **Cove Fort** (Rowley et al., 2013), **Desert Peak** (Benoit et al., 1982), **Dixie Meadows** (Delwiche et al., 2023), **Dixie Valley** (Blackwell et al., 1999; Benoit, 2015), **Don A. Campbell** (Orenstein et al., 2015), **The Geysers** (Beal and Box, 1991; Goyal, 1995; Garcia et al., 2012), **Heber** (Ramirez et al., 2023), **Ijen** (Libbey et al., 2026), **Jersey Valley** (Drakos et al., 2011), **Kamojang** (Zuhro, 2004; Kamah et al., 2005; Suryadarma et al., 2010; O'Sullivan et al., 2023b), **McGinness Hills** (Nordquist and Delwiche, 2013), **Mokai** (Moon et al., 2022), **Momotombo** (Porras and Itoi, 2006; Porras et al., 2007, Bjornsson, 2008; Porras and Bjornsson, 2010; Kaspereit et al., 2016), **Mount Apo** (Sambrano et al., 2010), **Mutnovsky** (Assaoulov, 1994; Kiryukhin et al., 2018); **Neal** (Murphy et al., 2021), **Ngā Tamariki** (Chambefort et al., 2016; Potter et al., 2020), **Olkaria West** (Rop, 2013; Jin, 2024), **Ormesa** (Ramirez et al., 2023), **Paisley** (Makovsky, 2013), **Patua** (Garg et al., 2015; Cladouhos et al., 2017; Murphy et al., 2017; Pollack et al., 2020; Smith et al., 2023), **Raft River** (Nash and Moore, 2012), **Reykjanes** (Friðleifsson et al., 2020), **Salak** (Stimac et al., 2008; Golla et al., 2020), **Salt Wells** (Hinz et al., 2014), **Salton Sea** (Hulen et al., 2002; Araya, 2022; O'Sullivan et al., 2023; Renaud et al., 2025; Sims et al., 2025), **San Jacinto** (Mackenzie et al., 2012; Pineda et al., 2020), **Soda Lake** (McLachlan, 2018), **Steamboat** (White, 1968; Feucht et al., 2023; Dhakal et al., 2025), **Sumikawa** (Garg et al., 1996; Ariki et al., 2000; Kondo et al., 2017), **Tiwi** (Menzies et al., 2014; Mejorada et al., 2020), **Tungsten Mountain** (Delwiche et al., 2018), **Tuscarora** (Kluge et al., 2025), and **Zunil** (Asturias, 2003).

2. TEMPERATURE

The natural-state temperatures within a geothermal system vary as a function of the fluid flow pathways, i.e., the upflow, outflow, and recharge geometry, and where applicable, the conductive heat transfer from upper crustal magmatic bodies. There is thus corresponding variability with the temperature and enthalpy of fluid produced from production wells within an individual geothermal field.

For the implemented approach, the *Temperature* parameter is defined as the amalgamated and mass-weighted production fluid temperature at the initial plant start-up. For single-phase, liquid-fed binary systems, this number is the average inlet temperature of a power plant at plant start-up. For two-phase developments, this *Temperature* parameter equates to the averaged feedzone formation temperatures, which may contain liquid, two-phase, or steam-dominated pore space conditions in the static state, and which may flow with varying degrees of excess enthalpy. There is inherently more uncertainty regarding the start-up *Temperature* parameter for *Calibration Analogs* with two-phase conditions, owing to the compounding uncertainties of P-T log equilibration, flowing enthalpy measurement accuracy, and degree of excess enthalpy from contributing steam zones.

The approach utilized herein defines *Temperature* as a deterministic variable for *Calibration Analogs*, whereas a probabilistic range of *Temperature* should be utilized for exploration-phase projects, considering insights provided by geothermometry, well measurements, and analog field comparisons. Following the conceptual development approach, consideration should also be given to the notion that the average start-up temperature of a geothermal field may be notably lower than the upflow temperature. Such is the case for systems that produce from both upflow and outflow regions (e.g., Amatitlan, Cove Fort, Momotombo, Mount Apo, Mutnovsky, Steamboat, Salak, and Tiwi; Table 1), as well as those that produce solely from the outflow (e.g., Salt Wells and Don A. Campbell; Table 1).

Many phenomena in a developed geothermal resource can contribute to the evolution of reservoir conditions over time, e.g., injection-related cooling, marginal recharge cooling, pressure decline and liquid-level changes, and steam zone expansion/dry-out/collapse. The combined effects of these phenomena can influence the production history, development strategy, and estimated *30-Year Average Power Capabilities* of the *Calibration Analogs* utilized in this study and they are thus also among the numerous factors that notably influence the calculated *Recovery Factors*. The relationship of temperature decline trends with *Permeability Regimes* is presented in Murphy and Libbey (2026) and highlights the ability of the proposed classification scheme to provide some predictive insight into a reservoir's response to production.

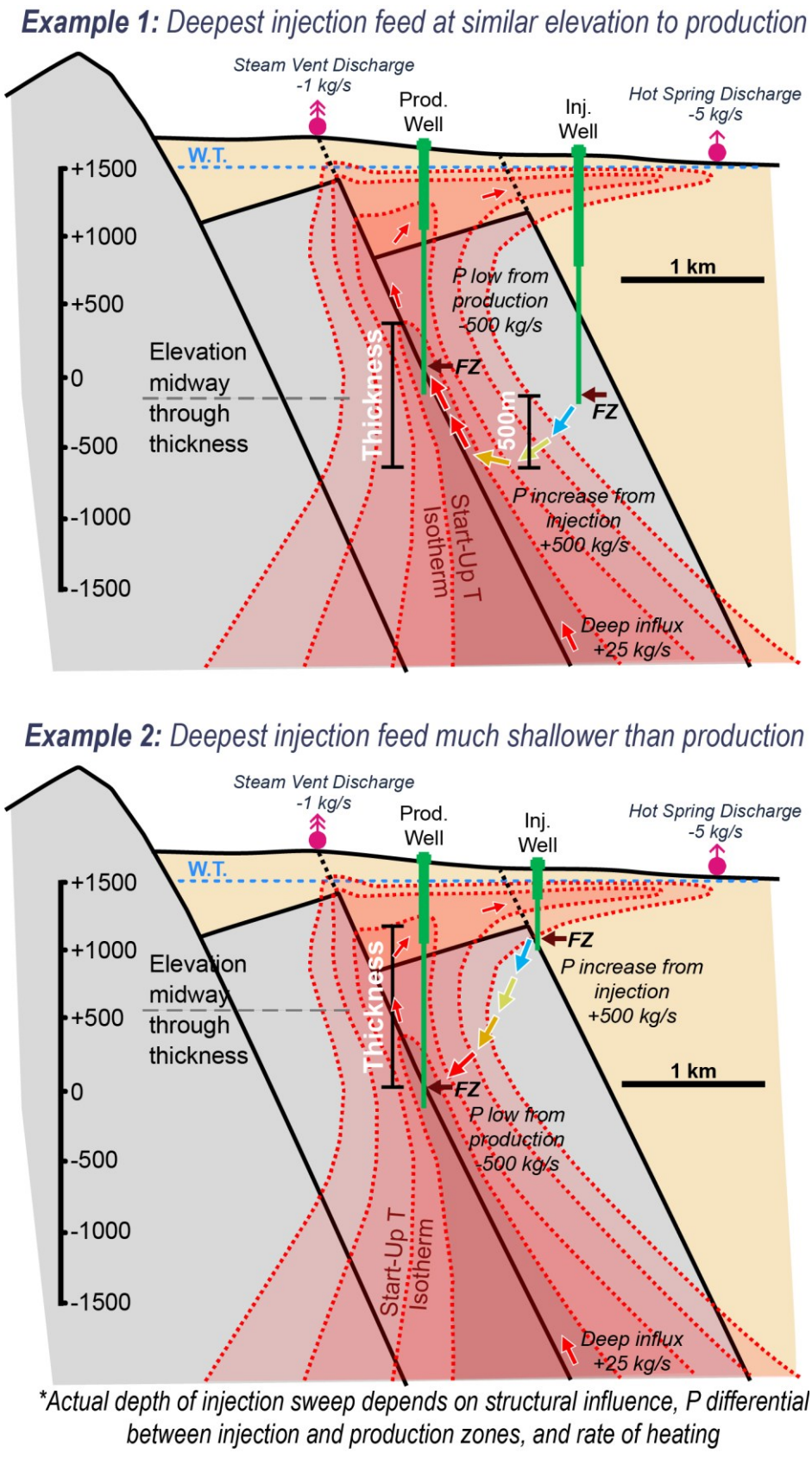

Figure 1. Schematics illustrating the *Thickness* definition utilized in this study, the impact of relative injection and production depths, and the method for selecting the elevation of the isotherms utilized in the *Area* definition.

3. THICKNESS

The *Thickness* parameter utilized in volumetric heat-in-place calculations is notoriously difficult to characterize, and many different definitions have been used in the industry, including those that define the thickness based on documented permeability, rock type, or the transition from conductive to convective temperature gradients (Grant, 2018).

The definition of *Thickness* proposed in this study is the vertical depth from the shallowest elevation of the mean or realized *Temperature* isotherm in natural state conditions to the base of notable production-injection heat-sweeping in a postulated or realized development (Figure 1). The depth of heat-sweeping of injection fluids likely depends on a myriad of parameters including structural permeability influences, pressure differential and distance/vertical offset between injection and production zones, and the rate of re-heating of injection fluids.

Some insight into the depth of heat-sweeping can be provided from tracer data, the geometry of cooling trends resolved from well logs and enthalpy monitoring data, and numerical models. Additionally, microseismic data have provided valuable insight into the geometry of injection heat-sweeping in numerous fields, however, there are also many examples where the results of these surveys are more cryptic, with uncertainties in subsurface velocity models potentially adding large error bars to the locations of resolved hypocenters.

Notwithstanding all of these complexities and ambiguities, a phenomenon that can be considered likely in most cases is some degree of density-driven injection fluid "sinking" below injection feedzone elevations. In absence of other information, the approach herein is to define the maximum depth of this density-driven injection fluid "sinking" as 500 mVD from the elevation of the deepest injection feedzone. While this may be an underestimation or overestimation of the actual depth of injection fluid circulation in a realized development, this approach attempts to standardize this otherwise often nebulous parameter.

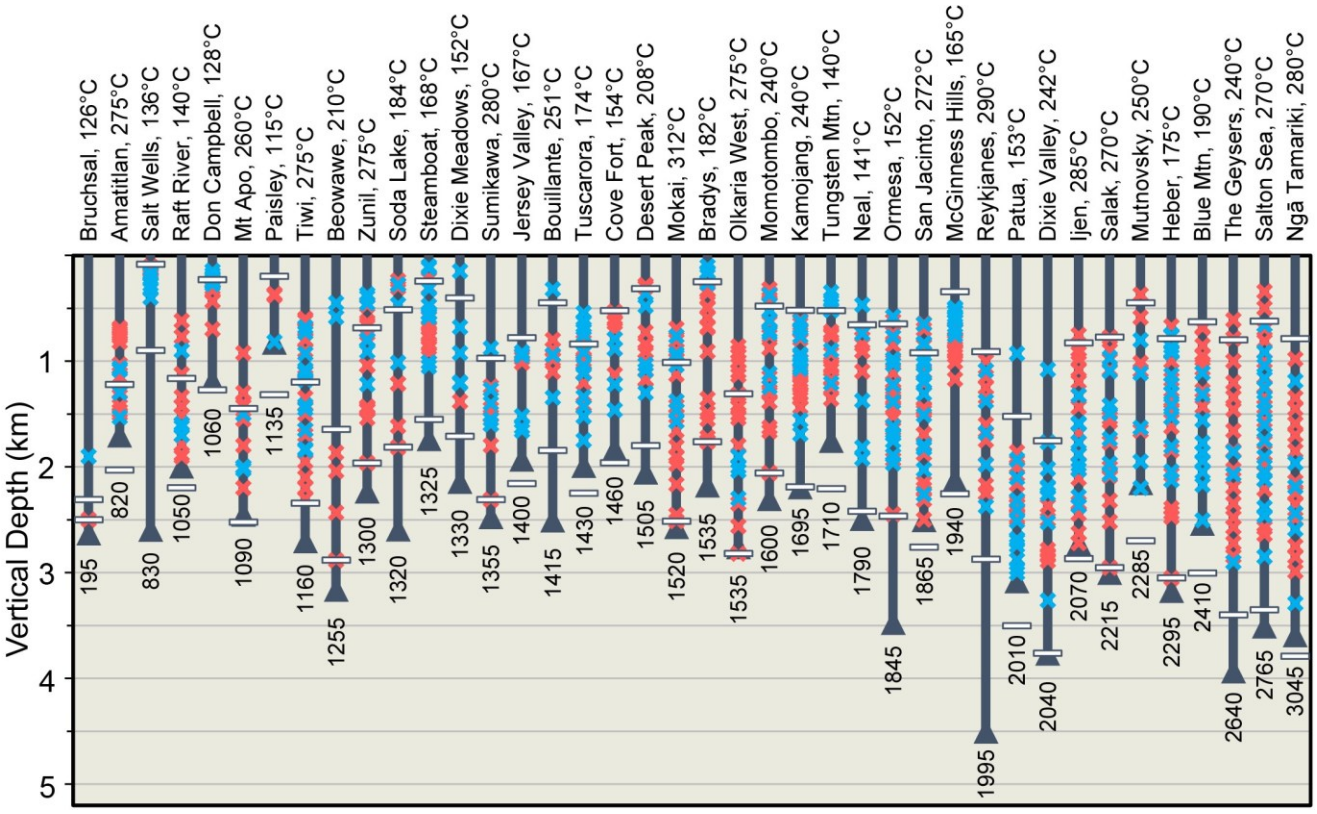

Figure 2. Representative vertical depths of production (red) and injection (light blue) feedzones in select geothermal systems, sorted by increasing mean *Thickness*. The maximum drilled vertical depth in each of these systems is displayed in dark blue. The calculated mean *Thickness* (in vertical meters) is displayed with text, with the top and bottom boundaries of this *Thickness* denoted by white bars. The elevation of the temperature isotherm that defines the top boundary of the *Thickness* is provided next to the field name along the top of the plot.

The calculated thickness for the *Calibration Analogs* is thus dependent on the relative depths of production and injection feedzones (Figure 1). In cases where the deepest injection feedzones are notably shallower than the deepest production feedzones (e.g., Beowawe, Brady, Momotombo, and Zunil), the base of the thickness is defined by the elevation of the deepest production feedzone (Figures 1 and 2). Conversely, where the deepest injection zones are <500 m shallower or where they are deeper than the deepest production feedzone, the base of the thickness is defined by 500 m below the deepest injection feedzone in the field (Figures 1 and 2; e.g., Amatitlan, Patua,

San Jacinto, and Ijen). This methodology assumes that the calculated thickness from this feedzone distribution and density-driven sinking assumption produces the P50 estimate of thickness for the field, with a P10 (reasonable maximum value) prescribed as P50*1.25 for each of the Calibration analogs. The P90 thickness and the Swanson's approximation of the mean are then computed, under the assumption that the *Thickness* parameter is a moderately skewed, lognormally distributed variable.

In cases where there is reliable evidence to support a base of heat-sweeping significantly below the deepest feedzones in a system, those supporting data can be utilized to define the base of the interval used to represent *Thickness*. An example of this is provided by McGinness Hills, where production and injection wells are situated on opposite sides of an accommodation zone (Figures 2 and 4), creating a fortuitous structural configuration of antithetically-dipping faults that facilitate the circulation of injection fluids ~1100 m below the deepest feedzone in the system. In this example, evidence for this deep heat-sweeping is provided by cooling trends in deep wells, tracer data, and numerical model simulations. Tungsten Mountain is another example where deep cooling trends, tracer data, and numerical model matches support ~1000 mVD of heat-sweeping below the deepest injection feedzone.

Following this definition of *Thickness*, end-member stratigraphic systems without notable convective fluid flow along faults are likely to have small thickness values, owing to the presence of dominantly conductive temperature gradients, and generally greater depths of drilling required to reach "economic" temperatures, as opposed to systems with notable convective flux. The varying *Thickness* values of Bruchsal, Germany (195 m thick; Figures 2, 3) versus systems in the Imperial Valley (typically >1800 m thick), illustrate this point for stratigraphic systems without and with notable components of convective fluid flux, respectively.

The mean *Thickness* values of all Calibration Analogs, and their P90-P10 ranges, are listed in Table 1 and displayed in Figure 3. 80% of the Calibration Analogs have thickness values between approximately 1050 and 2300 m, without a notable difference between *Permeability Regimes* (see Section 5), with the exception of Stratigraphic systems with minimal convective flux and dominantly conductive thermal gradients, as noted above. Considering these data, and following the described approach, a P90-P10 *Thickness* range of 1000-2300 mVD is herein considered reasonable to utilize for many exploration phase projects, in absence of any other constraining subsurface datasets and/or anticipated development strategies. The two strictly outflow developments in the *Calibration Analog* dataset, Salt Wells and Don A. Campbell, have *Thickness* values of 830 and 1030 m, respectively, and it is logical that thickness P90-P10 ranges for outflow exploration-phase targets should generally skew towards smaller values than those used in the resource capacity estimation of upflow or upflow + outflow exploration targets.

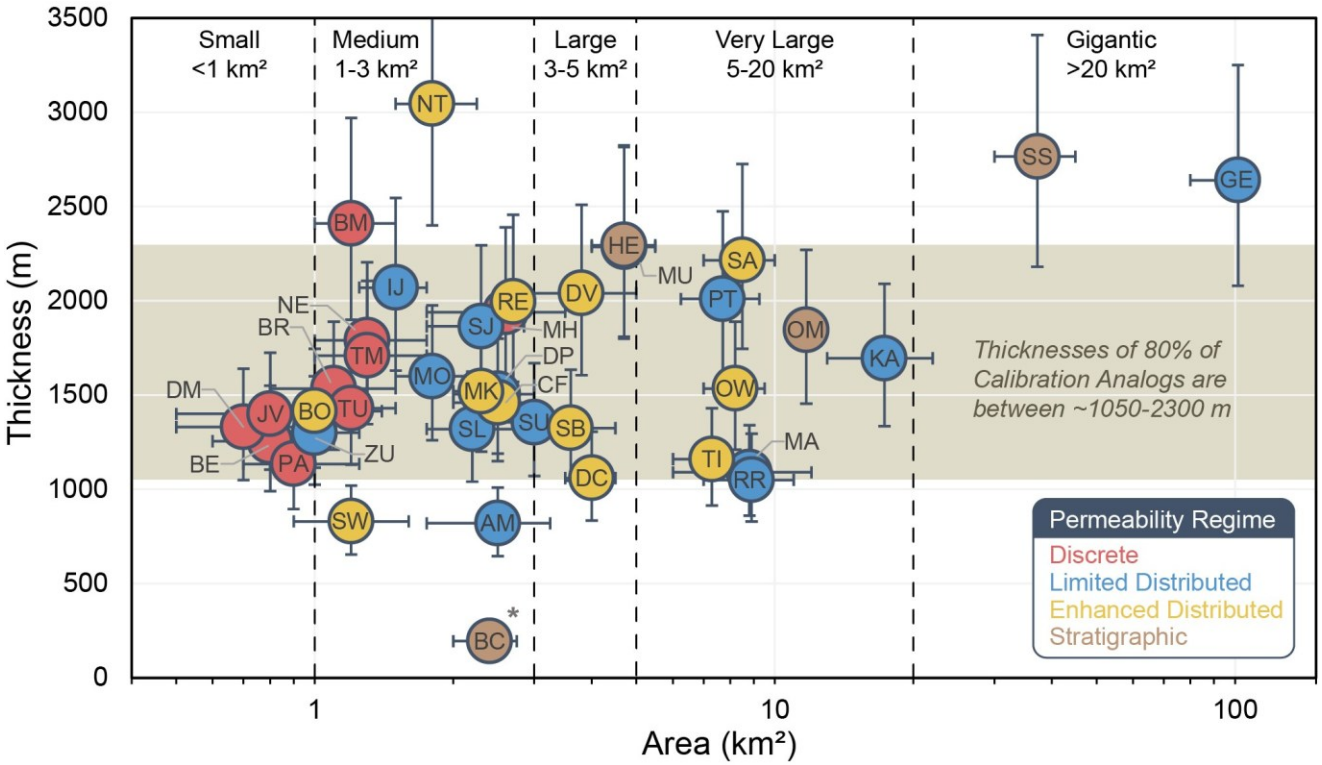

Figure 3. Estimated mean and P90/P10 (error bars) *Areas* and *Thicknesses* of *Calibration Analogs* used in this study. Fields colored by their characteristic Permeability Regime. *Bruchsal (BC) is a Stratigraphic system without notable convective heat flux – this is the one exception in the Calibration Analog dataset where *Area* was estimated using a merged 500 m buffer around the existing doublet injection and production wells (as opposed to the >>1000 km² area of >126°C temperatures at a halfway elevation through the resource thickness).

4. AREA

There are a wide range of *Area* definitions utilized in the geothermal industry, ranging from those that sum defined buffer areas around production wells (Wilmarth and Stimac, 2015; Grant, 2018) to approaches that aim to quantify the connected volume of a fractured reservoir. Area estimations are also sometimes drawn to encompass the distribution of thermal manifestations, mapped alteration, or the extent of low resistivity anomalies assumed to represent argillic alteration in association with an active geothermal system. As noted by Wilmarth et al. (2020), these latter methods of quantifying area often produce results that are not reflective of the subsurface extent or geometry of geothermal systems, nor do they empower meaningful analog comparisons or consistent approaches to capacity estimations.

The definition of resource *Area* utilized herein is the area of the natural-state isotherm of the mean estimated or realized start-up temperature for exploration phase and developed *Calibration Analogs*, respectively, at an elevation slice halfway through the defined *Thickness* (Figure 1). This method is a conceptual model-driven approach, which requires consideration of the likely geometry of subsurface isotherms. The approach to developing representative subsurface isotherm models are described in Cumming (2009, 2016), a process which involves the integrated interpretation of available P-T data, and geophysical, geochemical, and geological datasets. As with the other parameters discussed above, *Area* should be estimated in a probabilistic manner, with P90/P10 boundaries reflecting the existing uncertainty given the available surface and subsurface data and robustness of the conceptual model. While more involved than many other approaches for defining area, this framework for characterizing resource area aligns with a conceptual model and conceptual development approach, with the result being resource areas that meaningfully represent notable hydrological and permeability features of geothermal systems and that enable consistent field-to-field comparisons.

When following this standardized approach to characterizing *Area*, the relative size of a geothermal system can be interpreted as follows: <1 km^2 = *Small*; 1-3 km^2 = *Medium*; 3-5 km^2 = *Large*; 5-20 km^2 = *Very Large*; and >20 km^2 = *Gigantic*. Geothermal systems in each of these size categories are represented in the *Calibration Analog* dataset (Figure 3), and 1:90,000 summary maps of a selection of these fields are provided in Figure 4 to illustrate the wide range of geometries and sizes of geothermal systems across a diverse range of geologic settings. A detailed discussion of the geologic and hydrologic phenomena governing these resource geometries is beyond the scope of this paper, however, the maps in Figure 4 illustrate varying influences of permeability distribution, magmatic heat source proximity, and cold water recharge on the geometries and overall aerial extents of geothermal systems. For instance, amagmatic, deep-circulation systems hosted at structural discontinuities in rocks with otherwise low background permeability (e.g., Beowawe and Tuscarora) have small *Areas* and their geometries are notably elongated along structural trends. Marginal recharge profoundly influences the *Areas* of the Greater Olkaria field and Ijen by creating steep thermal gradients and system boundaries as cooler fluids migrate to depths along faults and the conduits of monogenetic volcanic features. Additionally, the Gigantic *Areas* of the Salton Sea and The Geysers are in large part related to the presence of extensive shallow to mid-crustal magmatic heat sources (Hulen et al., 2002; Karakas et al., 2017; Mitchell et al., 2023).

The *Areas* of geothermal resources in sedimentary basins can also be characterized following the above methodology, with some notable caveats. Sedimentary systems where there is an element of deep convection along basement structures, such as those found in the Imperial Valley, display highly elevated local thermal gradients within the sedimentary package and thus represent stratigraphic geothermal systems with definable boundaries. Such systems are thus well-suited to the described methodology of characterizing *Area*, and they often represent systems with large to very large *Areas* as a result of fluids spreading out over substantial lateral distances along subhorizontal (stratigraphic) permeability horizons. A complication to the proposed definition of *Area* is apparent with geothermal resources within sedimentary basins devoid of notable convective heat flow. In these settings, a specific target resource isotherm may persist over basin-scale areas (e.g., >1000 km^2) simply reflecting the regional background heat flow and thermal conductivity of the sedimentary package. In these settings, the basin-scale delineation of *Area*, following the methodology above, may still have scientific merit, however, the practical utility of this definition of *Area* to specific developments in these settings is lessened. For the purposes of resource capacity estimates, in these sedimentary systems that do not have localized anomalous thermal gradients above background, a more reasonable approach may be to utilize an area that encompasses a merged buffer around active production and injection wells in a development. An example of this is provided by Bruchsal, Germany, where the 126°C isotherm at an elevation of halfway through the resource thickness (-2200 mrsl) extends over an area >>1000 km^2 (Pester et al., 2010; Agemar et al., 2012, 2014a, 2014b). An illustration of this exception to the *Area* definition is provided in the bottom map of Figure 4, which displays the merged 2.4 km^2 area buffer around the production-injection doublet at Bruchsal.

An adjustment to the proposed *Area* definition presented above is also made for systems that dominantly produce (or that are expected to dominantly produce) from pronounced outflows. In these circumstances, the *Area* is defined as the area of the estimated or realized start-up temperature isotherm at the midway elevation through the outflow. Salt Wells and Don A. Campbell represent examples of outflow developments in the *Calibration Analog* dataset, with their mean *Areas* listed in Table 1 and depicted in Figure 4.

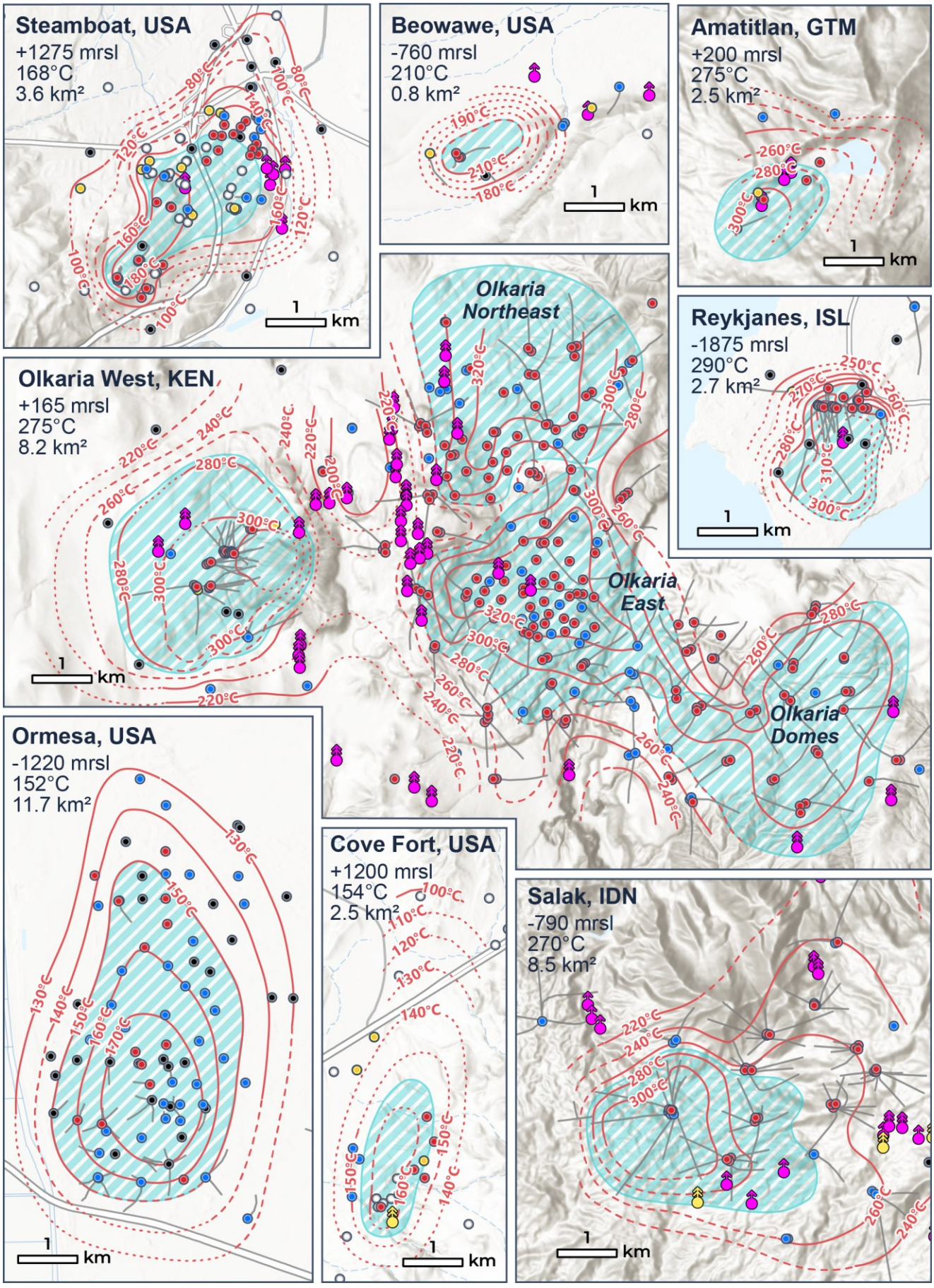
Steamboat, USA
+1275 mrsl
168°C
3.6 km²
Beowawe, USA
-760 mrsl
210°C
0.8 km²
Amatitlan, GTM
+200 mrsl
275°C
2.5 km²
Olkaria Northeast
Olkaria West, KEN
+165 mrsl
275°C
8.2 km²
Reykjanes, ISL
-1875 mrsl
290°C
2.7 km²
Olkaria East
Olkaria Domes
Ormesa, USA
-1220 mrsl
152°C
11.7 km²
Cove Fort, USA
+1200 mrsl
154°C
2.5 km²
Salak, IDN
-790 mrsl
270°C
8.5 km²
1 km

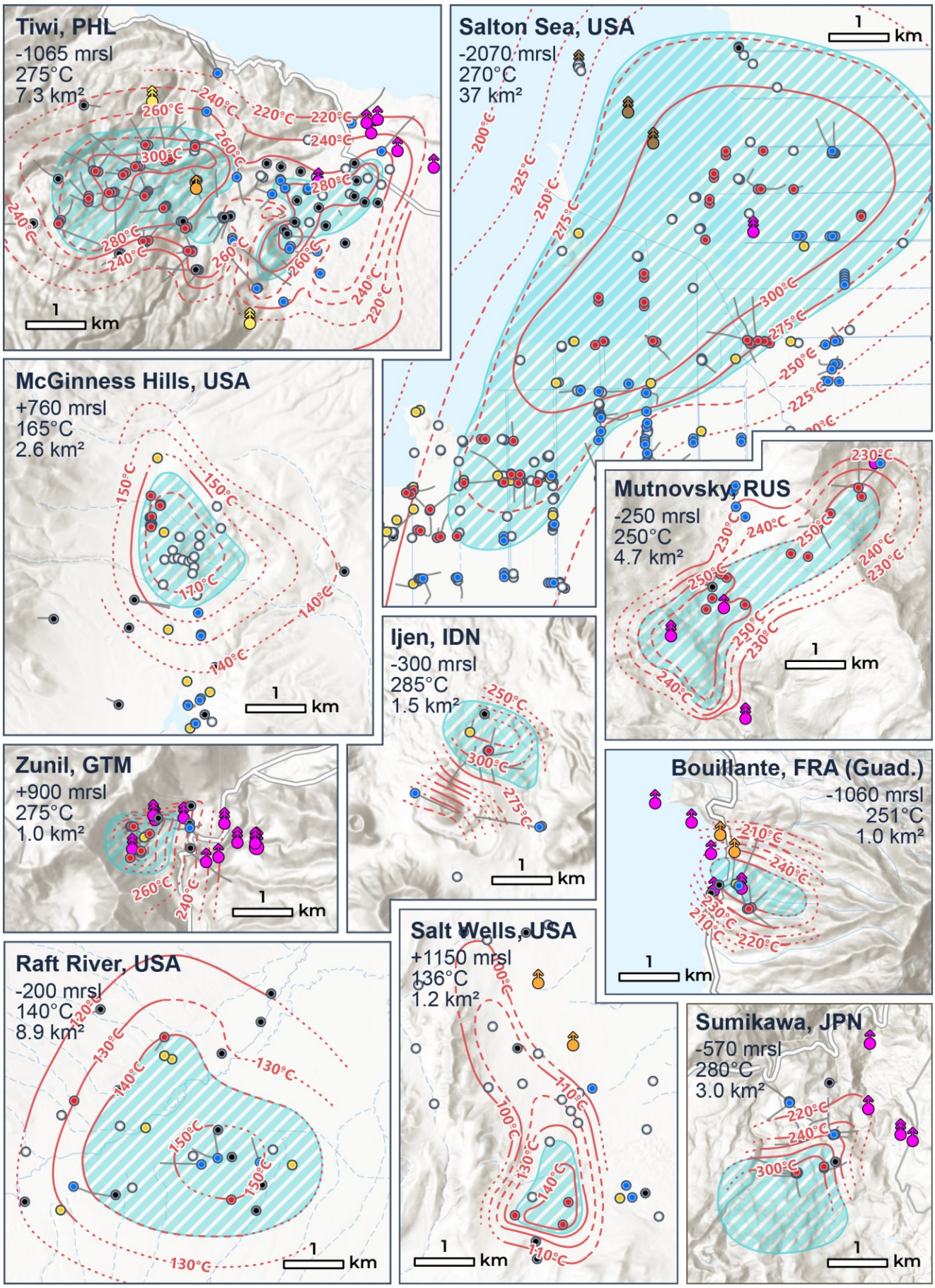
Tiwi, PHL
-1065 mrsl
275°C
7.3 km²
Salton Sea, USA
-2070 mrsl
270°C
37 km²
McGinness Hills, USA
+760 mrsl
165°C
2.6 km²
Mutnovsky, RUS
-250 mrsl
250°C
4.7 km²
Ijen, IDN
-300 mrsl
285°C
1.5 km²
Zunil, GTM
+900 mrsl
275°C
1.0 km²
Bouillante, FRA (Guad.)
-1060 mrsl
251°C
1.0 km²
Raft River, USA
-200 mrsl
140°C
8.9 km²
Salt Wells, USA
+1150 mrsl
136°C
1.2 km²
Sumikawa, JPN
-570 mrsl
280°C
3.0 km²
1 km

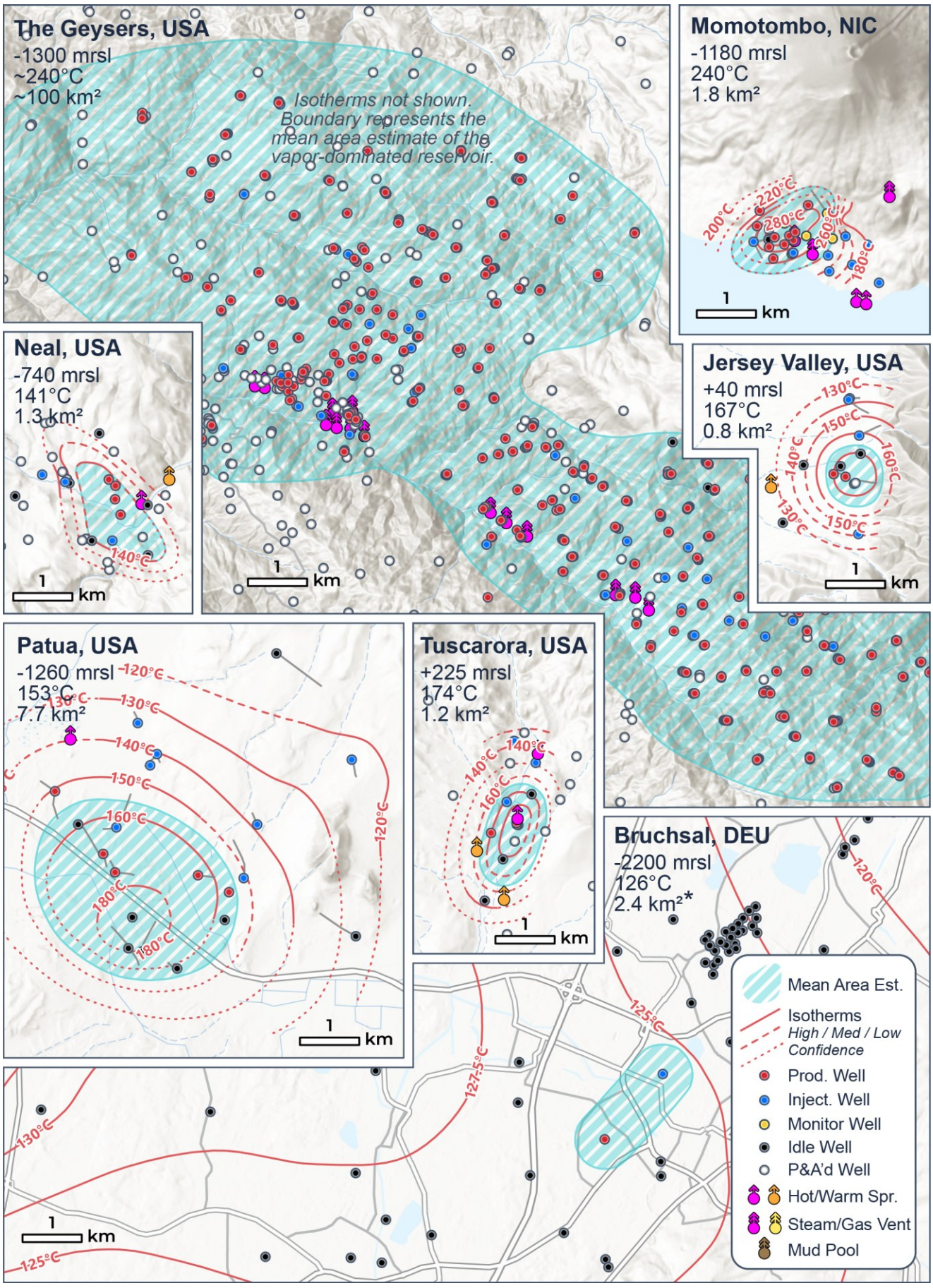
The Geysers, USA
-1300 mrsl
~240°C
~100 km²
Isotherms not shown. Boundary represents the mean area estimate of the vapor-dominated reservoir.
Momotombo, NIC
-1180 mrsl
240°C
1.8 km²
200°C
220°C
280°C
260°C
180°C
Neal, USA
-740 mrsl
141°C
1.3 km²
140°C
Jersey Valley, USA
+40 mrsl
167°C
0.8 km²
130°C
150°C
140°C
160°C
Patua, USA
-1260 mrsl
153°C
7.7 km²
120°C
130°C
140°C
150°C
160°C
180°C
Tuscarora, USA
+225 mrsl
174°C
1.2 km²
140°C
160°C
Bruchsal, DEU
-2200 mrsl
126°C
2.4 km²*
120°C
125°C
127.5°C
130°C
1 km
Mean Area Est.
Isotherms
High / Med / Low Confidence
Prod. Well
Inject. Well
Monitor Well
Idle Well
P&A'd Well
Hot/Warm Spr.
Steam/Gas Vent
Mud Pool

Figure 4. (Previous three pages) Isotherm maps and mean *Area* estimates for select geothermal systems of the *Calibration Analog* dataset used in this study. The elevations of the isotherms/resource *Area* are displayed on each map alongside the start-up *Temperatures* and mean *Area* estimate in km^2. All maps utilize the same scale (1:90,000) and projection (UTM WGS84 and their respective UTM zones) so that the portrayed geometries of the systems can be meaningfully compared.

5. PERMEABILITY REGIMES

The values, contrasts, and distribution of permeability within geothermal systems have profound effects on a system's size, hydrology, well flow capability, and response to production (Murphy and Libbey, 2026). Permeability facilitating convection in geothermal systems is a mix of primary (e.g., stratigraphic) and secondary (e.g., fracture-based) permeability, with the relative importance and mixture of these depending on, and often predictable based on, the geologic context of the system in question.

This study and a companion study by Murphy and Libbey (2026) have conducted a global review of geothermal systems and concluded that most systems comfortably fit within, or along the spectrum between, four end-member *Permeability Regimes*: Discrete, Limited Distributed, Enhanced Distributed, and Stratigraphic (Figure 5). In the discussion below, *matrix permeability* refers to connected primary porosity (e.g., connected pores between clasts) and sedimentary dissolution porosity (such as karst), whereas *background permeability* refers to the amalgamated matrix, contact-related, and distributed fracture permeability that is not directly associated with system-scale faults.

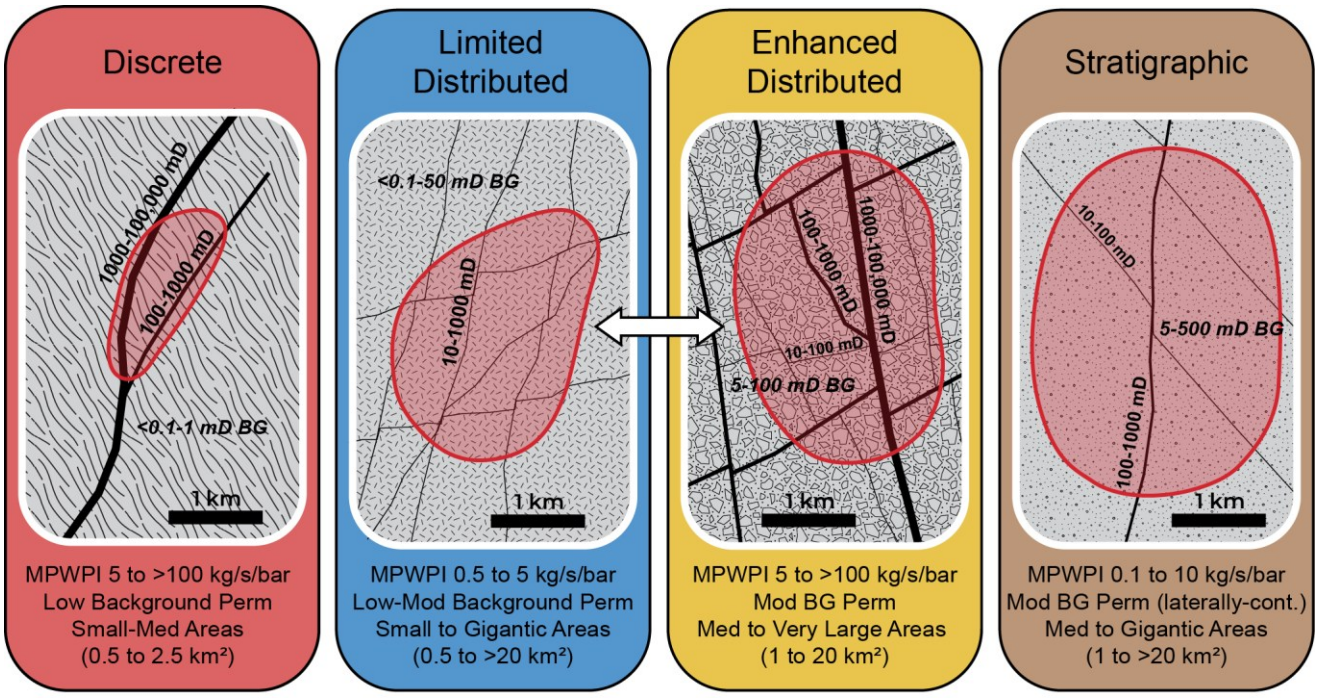

Figure 5. Plan-view generalized schematics of the four end-member Permeability Regimes of geothermal systems with representative ranges of background (BG), distinct fracture permeability, MPWPI, and likely resource *Area* ranges. The white arrow connecting Limited Distributed and Enhanced Distributed emphasizes that these end-member *Permeability Regimes* should be considered as a continuum.

5.1 Discrete

The Discrete *Permeability Regime* is characterized by settings exhibiting convection along localized fracture networks, within host rocks that have low background permeability (e.g., granites and many types of metamorphic rocks). The contrast of high permeability along structurally-controlled conduits with surrounding low background permeability creates geothermal systems with focused geometries (Wallis et al., 2015) and generally small to medium resource *Areas* of 0.5-2.5 km^2, often with anisotropic geometries conforming with the orientation of dominant structural controls. The specific favorable structural settings that host these Discrete permeability geothermal systems, and that are also applicable to other permeability types described below, have been elucidated by many studies in the Basin and Range and elsewhere (Rowland and Simmons, 2012; Faulds and Hinz, 2015; Faulds et al., 2021; Siler, 2023). The Discrete *Permeability Regime* is also characterized by the ability to obtain moderate to very high well permeabilities, within MPWPIs ranging from 5 to >100 kg/s/bar (Murphy and Libbey, 2026). Geothermal systems with Discrete *Permeability Regimes* can be found in a wide variety of geothermal province types, with notable examples in those characterized by regional continental extension, such as the Basin and Range, USA (e.g., Tuscarora, Beowawe, Neal, and Jersey Valley), the Western Chortis Block Extensional Province in Honduras and Guatemala (e.g., Platanares, Azacualpa, and Joaquina), and the Himalayan geothermal province in China and northern India (e.g., Yangbajain, Yangyi, and Manikaran).

5.2 Limited Distributed

The Limited Distributed *Permeability Regime* is characterized by less heterogeneity in the subsurface permeability structure than is intrinsic to Discrete settings, and correspondingly lower ratios of background permeability to feedzone permeability. As with the Discrete permeability type, specific structural discontinuities are likely to remain important for influencing the location of these systems, alongside other potential factors such as the existence of magmatic heat sources and the influences of cold water hydrology, however, a notable amount of feedzones for wells in these fields are from distributed networks of fractures that do not represent (or at least are not easily relatable) to specific system-scale structures within the resource area. Other elements of the subsurface geologic sequence, such as brecciated lavas and lithologic contacts may also provide quantifiable contributions to a well's overall permeability in these Limited Distributed settings. Fluid contained within the background permeability of these systems represent storage which supports flow along the higher permeability fractures that constitute feedzones (Wallis et al., 2015). Well permeability values in Limited Distributed settings are characteristically lower on average than those in Discrete permeability environments, with MPWPIs commonly ranging from 0.5 to 5 kg/s/bar. The *Areas* of geothermal resources with this *Permeability Regime* are widely variable, from <1 km^2 to >100 km^2, the upper end of these which constitute the largest identified convective geothermal systems on the planet (e.g., The Geysers and Larderello). Limited Distributed geothermal systems can occur in a very wide variety of geologic environments including volcanic arcs (e.g., Zunil, Ijen, Kamojang, Momotombo, and Sumikawa), zones of passive regional continental extension (e.g., Patua, Raft River, Desert Peak), and regions of post-orogenic magmatism (e.g., Larderello and The Geysers).

5.3 Enhanced Distributed

The Enhanced Distributed *Permeability Regime* shares some characteristics of the Limited Distributed systems, in that a notable amount of the convective flow of the system occurs within the background permeability of the host rocks as well as along system-scale structures. However, the average background permeability and feedzone-related permeabilities in these types of systems are higher than that found in the Limited Distributed settings, with MPWPIs ranging from 5 to >100 kg/s/bar. It is reasonable to consider the Limited Distributed and Enhanced Distributed *Permeability Regimes* as representing a continuum, but to facilitate the characterization of resources, a minimum threshold MPWPI for the Enhanced Distributed category has been defined as 5 kg/s/bar. As with Limited Distributed fields, Enhanced Distributed settings can result in a wide range of resource *Areas*, with the majority of systems in the *Calibration Analog* dataset represented by medium to very large areas (Figure 3). A wide variety of geothermal province types can host Enhanced Distributed systems, but notable examples are found in zones of active rifting (e.g., Olkaria and Reykjanes), extensional or transtensional volcanic arcs/backarcs (e.g., Bouillante, Salak, Mindanao, Ulubelu, and Ngā Tamariki), regions of post-orogenic magmatism (e.g., Mammoth), and provinces of passive regional continental extension (e.g., Steamboat, Salt Wells, Don A. Campbell, and Cove Fort).

5.4 Stratigraphic

The Stratigraphic *Permeability Regime* defines geothermal settings where the dominant permeability is associated with the matrix of laterally continuous sedimentary strata. In an end-member scenario devoid of notable fracturing, vertical permeability and corresponding upward convective flow can be limited in these settings as a result of layered permeable and impermeable strata, with the result being relatively conductive thermal gradients reflective of background heat flow values, the thermal conductivity of the rock, and potential deep convective input from fluid rising along fractured basement rock into the overlying strata. The existence of matrix-based laterally-continuous permeability horizons in these settings results in geothermal fields that spread out over large *Areas*, commonly >5 km^2, with impressive examples such as the Salton Sea geothermal field reaching a size of ~37 km^2 (Figures 3 and 4). In many Stratigraphic geothermal settings, such as sub-regions of the Salton Trough, the Rhine Graben, and the Pannonian Basin, faulting within the sedimentary strata facilitates a component of convection (Hulen et al., 2003; Baillieux, 2012; Haffen et al., 2013; Vidal and Genter, 2018), and sensu stricto such systems should be characterized as hybrid Stratigraphic-Limited/-Enhanced Distributed permeability settings (see discussion of *Hybrid Permeability Regimes*, below). However, considering the high ratio of matrix-related feedzone permeability relative to fracture-based permeability in these systems (Ramirez et al., 2023; Murphy and Libbey, 2026), geothermal systems such as Heber, the Salton Sea, Ormesa, and Cerro Prieto are more Stratigraphic in character than they are Distributed, following the definitions provided herein.

5.5 Hybrid and Coupled Permeability Regimes

While the majority of geothermal systems can be appropriately characterized within the framework of these four *Permeability Regime* end-members, some fields are better characterized by a hybrid of two of these end members (Figure 6) – as is illustrated above by the discussion of geothermal fields in the Imperial Valley.

Additionally, it is possible for an individual geothermal system to be characterized by multiple *Permeability Regimes* across different sub-regions of the field (Figure 7). These coupled permeability types can occur as a result of notable changes in host rock primary permeability and/or fracture density/character along the convective flow path of a geothermal system. An illustrative example of a *Coupled Permeability Regime* in a geothermal system is provided by Cove Fort, where a Discrete upflow along a structural discontinuity in granitic host rock transfers to an Enhanced Distributed outflow hosted within overlying fractured carbonate and siliciclastic sequences. Another example of a *Coupled Permeability Regime* is provided by the Stillwater system in Nevada, which displays fracture-based Limited Distributed permeability in the deeper Tertiary volcanic rocks and Stratigraphic permeability in sands of the overlying basin-fill – both which constitute important permeability features for production and injection within the field.

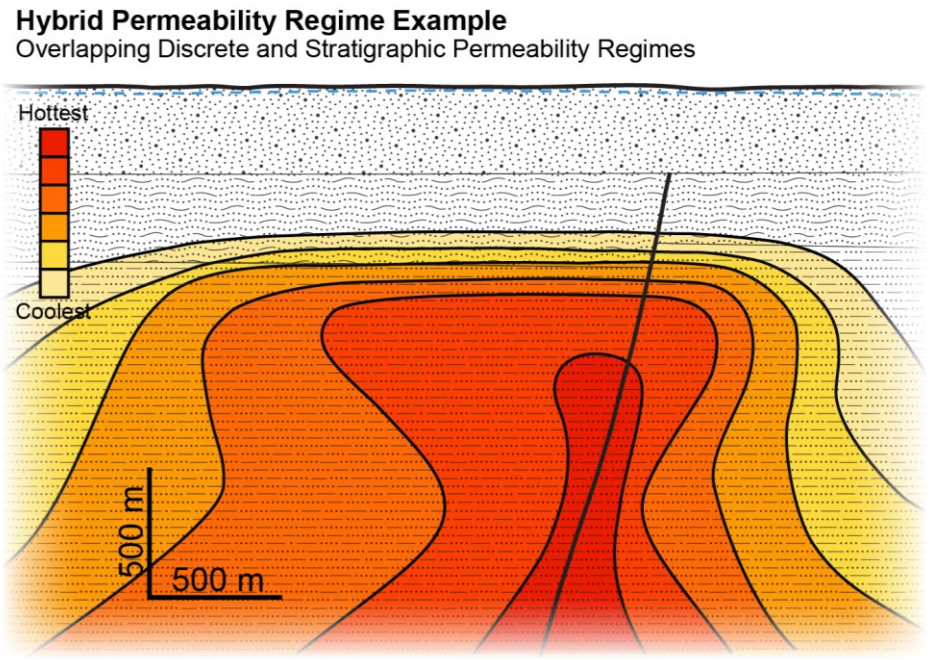

Figure 6. Idealized cross-section of a geothermal system with a Hybrid Permeability Regime. Modelled after Heber in the Imperial Valley (Ramirez et al., 2023).

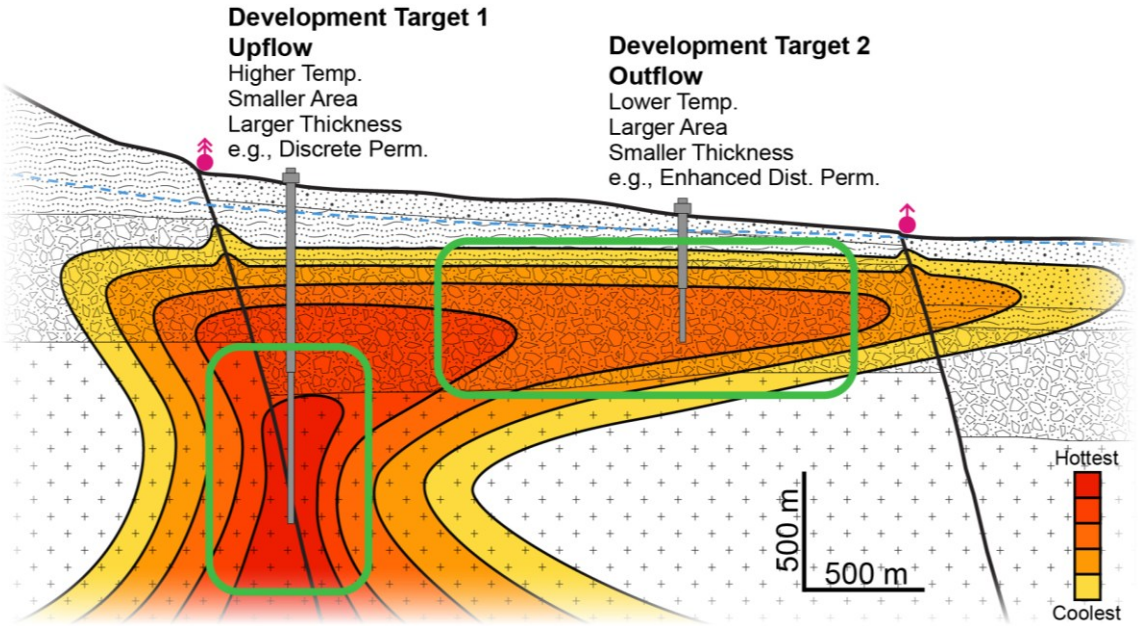

Figure 7. Idealized cross-section of a geothermal system with a *Coupled Permeability Regime* illustrating the significance of the "Conceptual Development Approach" described in the text.

5.6 The Relationship of Permeability Regimes to Recovery Factors

There are numerous definitions for *Recovery Factors* utilized by the geothermal industry, but in essence they are variables integrated into volumetric heat-in-place capacity estimation equations that aim to represent the *extractable heat energy* in a subsurface volume relative to the *total heat energy* contained in that volume, expressed as a percentage. As illustrated by Parini and Riedel (2000), parameters related to energy storage (e.g., porosity and temperature), parameters related to fluid recovery (e.g., fracture permeability, fracture spacing), and the impact of production-injection configurations can all influence the *Recovery Factors* of geothermal developments.

Recovery Factors calculated for the *Calibration Analogs* in this study range from ~4% (Raft River and Patua) to 53% (Salt Wells), with median and mean values of 16% and 19%, respectively for all forty of the studied fields. The higher-end *Recovery Factor* values of this dataset are supported by theoretical models discussed in Nathenson (1975), Garg and Pritchett (1990), and Sanyal and Butler (2005) that note the possibility of obtaining *Recovery Factors* that are 50% or higher. Despite following different approaches for characterizing resource geometries and power generation, the *Recovery Factors* computed in this study align closely with those reported in Grant (2018), namely the values using the "Tight" area definition and ambient reference temperature reported in that study, e.g.: 18% *Recovery Factor* versus 14% computed herein for Momotombo; 14% versus 19% for Ngā Tamariki; 11% versus 6% for the Geysers; and 20% versus 27% for Brady.

Recovery Factors for *Calibration Analogs* utilized in this study display a positive correlation with MPWPIs, as displayed on the *Recovery Factor* vs Log MPWPI plot shown in Figure 8. Additionally, these data reveal distinct data clusters corresponding to the four end-member *Permeability Regimes* described in this paper. Five *Calibration Analogs* in this study are computed to have very high Recovery Factors ranging from 40 to 53%. These fields all have very high MPWPI values, >60 kg/s/bar, and are characterized by Discrete and Enhanced Distributed *Permeability Regimes*. Conversely, the five lowest *Recovery Factors* computed in this dataset correspond to systems with MPWPIs ≤1 kg/s/bar and that are exclusively characterized by Limited Distributed *Permeability Regimes*.

These results suggest that if the proposed methodology for defining *Temperature*, *Thickness*, and *Area* are utilized as described in this paper, then estimates of MPWPI, or in absence of that, simply the characterization of a system's likely *Permeability Regime*, can inform the appropriate range of *Recovery Factors* to utilize in volumetric heat-in-place calculations. Probabilistic ranges of *Recovery Factors*, rather than a single deterministic value, should be used in such Monte Carlo based heat-in-place calculations to account for the variability visualized along the data trend in Figure 8, some of which may be related to the other variables that influence *Recovery Factors*, such as those examined by Parini and Riedel (2000) and listed above. Recommendations for reasonable P90-P10 values of *Recovery Factors* for different ranges of anticipated MPWPIs are provided at the top of Figure 8.

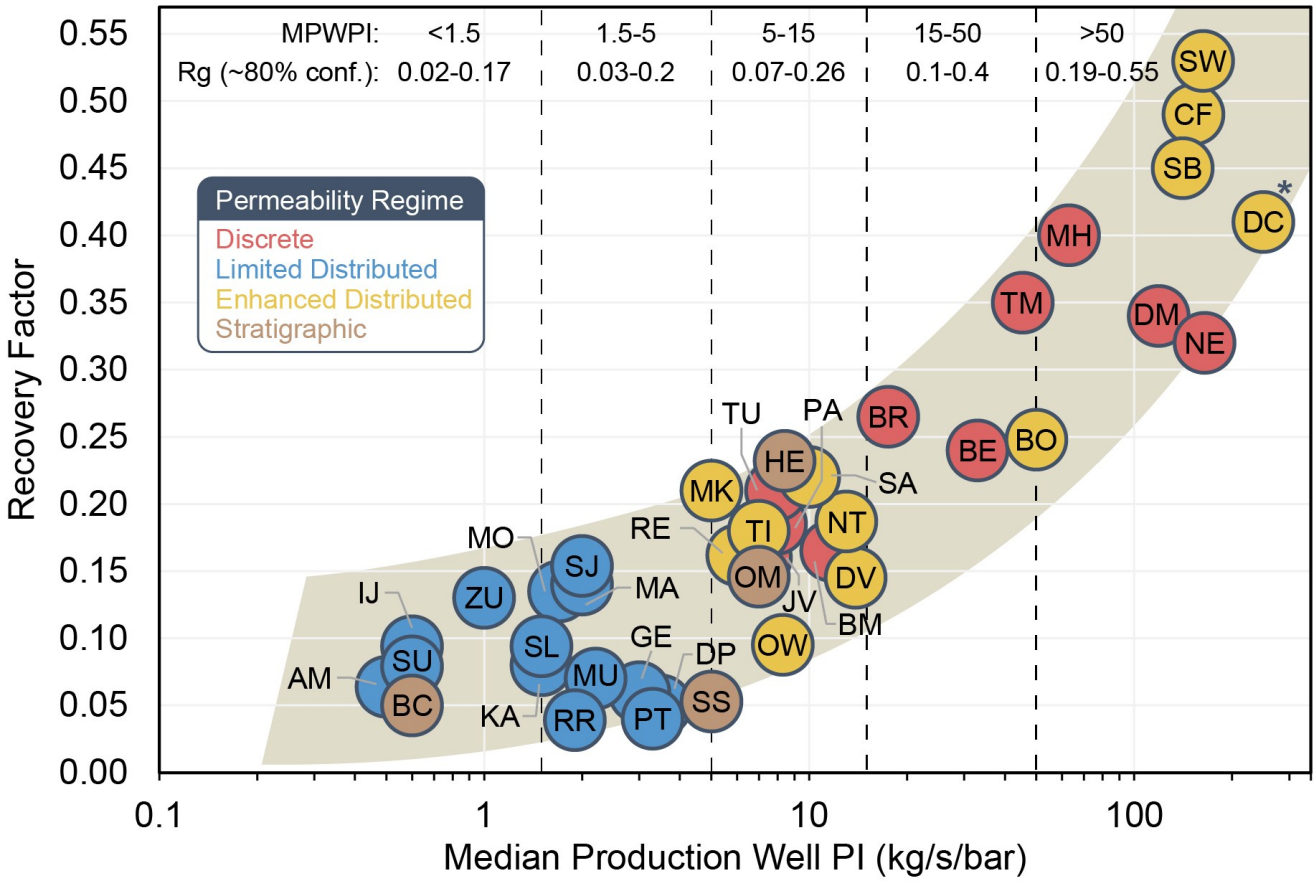

Figure 8. *Recovery Factors* versus MPWPIs for the *Calibration Analogs* utilized in this study. The MPWPI of Don A. Campbell is capped to 250 kg/s/bar, although data suggests this value is likely to be >1000 kg/s/bar. Reasonable values of P90-P10 *Recovery Factors* for different MPWPI ranges are provided at the top of the figure.

5.7 Area-Power Density

Area-power density methods are widely employed in the geothermal industry for making resource capacity estimates, especially for early-stage exploration projects. While compelling for their simplicity, published trends of MW/km^2 versus resource temperature have a large degree of scatter that calls into question their predictive capabilities (Holmes and Huebner, 2025). A plot of area-power density versus field start-up temperature for the *Calibration Analog* dataset utilized in this study is provided in Figure 9. The four fields with the highest power densities, 43-69 MW/km^2 (Reykjanes, Salak, Mokai, Ngā Tamariki) are all 270+°C systems with Enhanced Distributed *Permeability Regimes*. Conversely, the seven fields in the dataset with *Temperatures* <150°C all display comparatively low power densities of 0.2 to 20 MW/km^2. Power densities for 80% of the *Calibration Analog* dataset range from 5.6 to 38.5 MW/km^2, and aside from the upper- and lower-end subsets mentioned, these data lack any notable trends that could be considered applicable for robust resource capacity estimations. The results suggest that stochastic volumetric heat-in-place methods that consider *Permeability Regimes*, and that utilize standardized variable definitions, are a more informative approach for making resource capacity estimates, as they capture the combined geometry (area and thickness), permeability, and enthalpy aspects of the subsurface that are all major influences on the extractable amount of energy in geothermal systems.

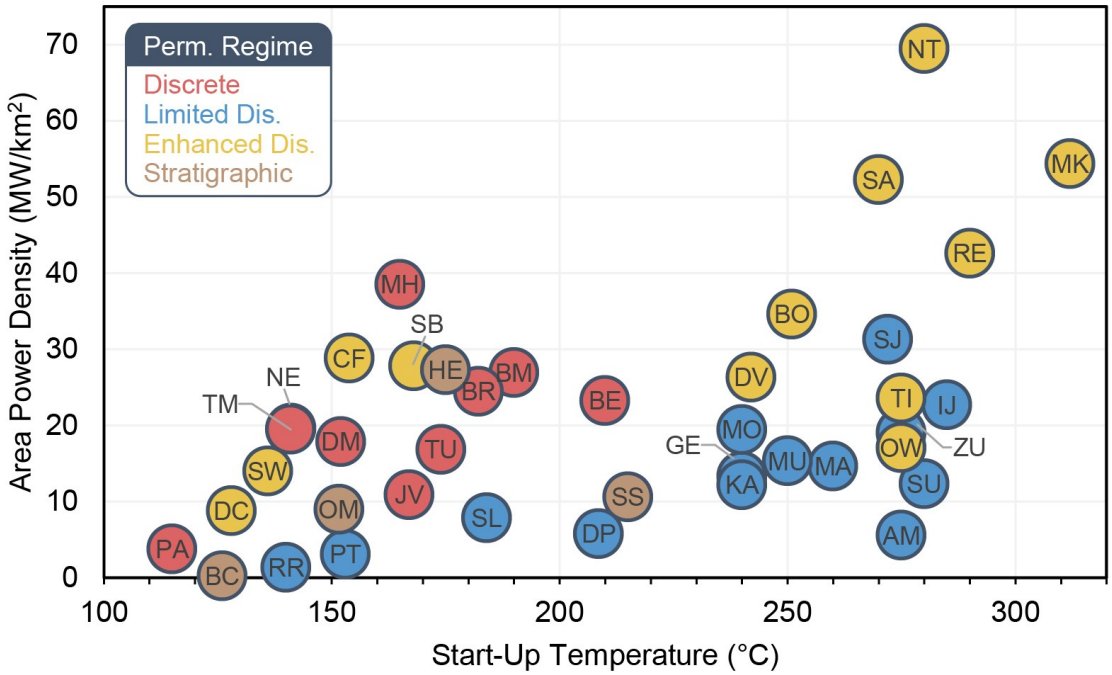

Figure 9. Area-power density versus field *Temperature* (at start-up) for *Calibration Analogs* utilized in this study. The calculated power density utilizes the estimated *30-Year Average Power Capability* for each field, as described in Section 1.3.

6. CONCLUSIONS

Proposed standardized definitions of key geothermal resource parameters, *Temperature*, *Thickness*, *Area*, and *Permeability Regime*, are detailed in this study. This schema is shown to have applicability for increasing the consistency of resource capacity estimations and optimizing the process of identifying relevant analogs by defining a common lexicon for key resource attributes. Additionally, a strong positive correlation between well permeabilities and *Recovery Factors* suggest that insight into the *Permeability Regime* and/or estimated production well PIs can meaningfully inform appropriate ranges of *Recovery Factors* to employ in volumetric heat-in-place capacity estimations. As with all capacity estimation approaches, sound conceptual models and a comprehensive review of relevant analogs are essential for defining reasonable P90-P10 ranges for parameters utilized in such equations.

DISCLAIMER AND ACKNOWLEDGEMENTS

The authors endeavored to accurately characterize the studied systems using the available data but acknowledge that many details of each system are approximate or may not accurately reflect the most up-to-date resource understanding. Support and corrections to improve on the existing *Calibration Analog* dataset are gladly welcomed.

The authors give sincere thanks to Ormat Technologies Inc., and specifically Simon Webbison, for supporting the publication of this study. This work has greatly benefited from collaboration with the many talented engineers and geoscientists of the Ormat Resource Group and thoughtful reviews by Bill Cumming and Greg Ussher.

REFERENCES

Agemar, T., Schellschmidt, R., & Schulz, R. (2012). Subsurface temperature distribution in Germany. Geothermics, 44, 65–77.

Agemar, T., Alten, J.-A., Ganz, B., Kuder, J., Kühne, K., Schumacher, S., & Schulz, R. (2014a). The Geothermal Information System for Germany – GeotIS. Zeitschrift Der Deutschen Gesellschaft Für Geowissenschaften, 165(2), 129–144.

Agemar, T., Weber, J., & Schulz, R. (2014b). Deep geothermal energy production in Germany. Energies, 7(7), 4397–4416.

Ariki, K., Kato, H., Ueda, A., & Bamba, M. (2000). Characteristics and management of the Sumikawa geothermal reservoir, northeastern Japan. Geothermics, 29, 171–189.

Araya, N. (2022). A 3D Conceptual and Natural-State Model of the Salton Sea Geothermal Field [Master of Engineering Thesis]. The University of Auckland.

Assaoulov, S. (1994). A conceptual model and reservoir assessment for the Mutnovsky geothermal field, Kamchatka, Russia. United Nations Geothermal Training Programme, 30 p.

Asturias, F. (2003). Reservoir assessment of Zunil I & II geothermal fields, Guatemala. United Nations Geothermal Training Programme, 32 p.

Baillieux, P. (2012). Multidisciplinary approach to understand the localization of geothermal anomalies in the Upper Rhine Graben from regional to local scale [PhD Thesis, Université de Neuchâtel].

Beall, J. J., & Box, W. T. (1991). The nature of steam-bearing fractures in the South Geysers reservoir. Geothermal Resources Council, Monograph on the Geysers Geothermal Field, Special Report, (17).

Benoit, D., Hiner, J. E., & Forest, R. T. (1982). Discovery and geology of Desert Peak geothermal field (Nevada Bureau of Mines and Geology Bulletin 97; p. 101 p). University of Nevada Reno.

Benoit, D. (2015). A Case History of the Dixie Valley Geothermal Field, 1963–2014. GRC Transactions, 3–11.

Bjornsson, G. (2008). Review of generating capacity estimates for the Momotombo geothermal reservoir in Nicaragua. GRC Transactions, 341–345.

Blackwell, D. D., Wisian, K. W., Benoit, D., & Gollan, B. (1999). Structure of the Dixie Valley geothermal system, a "typical" Basin and Range geothermal system, from thermal and gravity data. GRC Transactions, 23, 525–531.

Chambefort, I., Buscarlet, E., Wallis, I. C., Sewell, S., & Wilmarth, M. (2016). Ngatamariki geothermal field, New Zealand: Geology, geophysics, chemistry and conceptual model. Geothermics, 59, 266–280. https://doi.org/10.1016/j.geothermics.2015.07.011

Cladouhos, T. T., Uddenberg, M. W., Swyer, M. W., Nordin, Y., & Garrison, G. H. (2017). Patua geothermal geologic conceptual model. GRC Transactions, 41, 19 p.

Cumming, W. (2009). Geothermal Resource Conceptual Models Using Surface Exploration Data. Proc. Thirty-Fourth Workshop on Geothermal Reservoir Engineering, 6 p.

Cumming, W. (2016). Resource conceptual models of volcano-hosted geothermal reservoirs for exploration well targeting and resource capacity assessment: Construction, pitfalls and challenges. GRC Transactions, 40, 623–638.

Delwiche, B., Peters, B., Sophy, M., Smith, C., & O'Brien, J. (2018). Successful deployment of a multi-crossing directional drilling method at Ormat's new Tungsten Mountain geothermal field in Churchill County, Nevada. Proc. 43rd Workshop on Geothermal Reservoir Engineering, 15 p.

Delwiche, B., Libbey, R., Folsom, M., Johnson, A., Murphy, J., Zuza, R., Reno, P. S., & Usa, N. (2023). Exploration history and conceptual model of the Dixie Meadows geothermal field, Nevada, USA. Proceedings World Geothermal Congress 2023, 19 p.

Dhakal, S., Spake, D., Lee, L., Feucht, D., Murphy, J., Akerley, J., Johnson, A., Libbey, R., & Spielman, P. (2025). Forty years of production from the Steamboat geothermal field: Numerical model update. Proc. 50th Workshop on Geothermal Reservoir Engineering, 17 p.

Drakos, P., Spielman, P., & Björnsson, G. (2011). Jersey Valley exploration and development. GRC Transactions, 751–760.

Faulds, J., & Hinz, N. (2015). Favorable tectonic and structural settings of geothermal systems in the Great Basin region, western USA: proxies for discovering blind geothermal systems. Proc. World Geothermal Congress, 6 p.

Faulds, J. E., Coolbaugh, M., & Hinz, N. H. (2021). Inventory of structural settings for active geothermal systems and late Miocene (~8 Ma) to Quaternary epithermal mineral deposits in the Basin and Range province of Nevada (No. 58; Nevada Bureau of Mines and Geology Report, p. 27 p).

Fercho, S., Norbeck, J., Mcconville, E., Hinz, N., Wallis, I., Titov, A., Agarwal, S., Dadi, S., Gradl, C., Baca, H., Eddy, E., Lang, C., Voller, K., & Latimer, T. (2023). Geology, state of stress, and heat in place for a horizontal well geothermal development project at Blue Mountain, Nevada. Proc. 48th Workshop on Geothermal Reservoir Engineering, 16 p.

Feucht, D., Gates, C., Selwood, R., Churchill, M., & Zuza, R. (2023). Magnetotelluric data acquisition in a high-noise environment: Results from the Steamboat Hills geothermal complex, Nevada, USA. GRC Transactions, 47, 20 p.

Friðleifsson, G. Ó., Elders, W. A., Zierenberg, R. A., Fowler, A. P. G., Weisenberger, T. B., Mesfin, K. G., Sigurðsson, Ó., Níelsson, S., Einarsson, G., Óskarsson, F., Guðnason, E. Á., Tulinius, H., Hokstad, K., Benoit, G., Nono, F., Loggia, D., Parat, F., Cichy, S. B., Escobedo, D., & Mainprice, D. (2020). The Iceland Deep Drilling Project at Reykjanes: Drilling into the root zone of a black smoker analog. Journal of Volcanology and Geothermal Research, 391, 19 p.

Garg, S.K., and & Pritchett, J.W. (1990) Cold water injection into single- and two-phase geothermal reservoirs. Water Resources Research, v. 26(2), 331-338.

Garg, S., Pritchett, J., Stevens, J., Luu, L., & Combs, J. (1996). Development of a geothermal resource in a fractured volcanic formation: Case study of the Sumikawa Geothermal Field, Japan (SAND--96-2556, 446314; p. SAND--96-2556, 446314).

Garg, S. K., Goranson, C., Johnson, S., & Casteel, J. (2015). Reservoir Testing and Modeling of the Patua Geothermal Field, Nevada, USA. Proc. World Geothermal Congress, 16 p.

Garcia, J., Walters, M., Beall, J., Hartline, C., Pingol, A., Pistone, S., Goyal, K., Wright, M., & Conant, T. (2012). Overview of the Northwest Geysers EGS Demonstration Project. Proc. Thirty-Seventh Workshop on Geothermal Reservoir Engineering, 11 p.

Golla, G. U., Julinawati, T., Putri, R. P., Nordquist, G. A., Libert, F. T., & Suminar, A. R. (2020). The Salak Field, Indonesia: On to the next 20 years of production. Geothermics, 83, 15 p.

Goyal, K. P. (1995). Injection recovery factors in various areas of the Southeast Geysers, California. Geothermics, 24(2), 167–186.

Grant, M. A. (2018). Stored heat and recovery factor reviewed. Proc. 43rd Workshop on Geothermal Reservoir Engineering, 8 p.

Haffen, S., Geraud, Y., Diraison, M., & Dezayes, C. (2013). Fluid-Flow Zones in a Geothermal Sandstone Reservoir: Localization From Thermal Conductivity and Temperature Logs, Borehole EPS1 (Soultz-sous-Forêts, France). Proc. Thirty-Eighth Workshop on Geothermal Reservoir Engineering, 9 p.

Hinz, N. H., Faulds, J. E., & Coolbaugh, M. F. (2014). Association of fault terminations with fluid flow in the Salt Wells geothermal field, Nevada, USA. GRC Transactions, 3–10.

Herzberger, P., Münch, W., Kölbel, T., Bruchmann, U., Schlagermann, P., Hötzl, H., Wolf, L., Rettenmaier, D., Steger, H., Zorn, R., & Seibt, P. (2010). The Geothermal Power Plant Bruchsal. Proc. World Geothermal Congress, 6 p.

Hulen, J., Kaspereit, D., Norton, D. L., Osborn, W., & Pulka, F. S. (2002). Refined Conceptual Modeling and a New Resource Estimate For the Salton Sea Geothermal Field, ImperialValley, California. GRC Transactions, 26, 29–36.

Hulen, J. B., Norton, D. L., Moore, J. N., Osborn, W., & van de Putte, T. (2003). The role of sudden dilational fracturing in evolution and mineralization of the southwestern Salton Sea geothermal system, Imperial Valley, California. Proc. Twenty-Eighth Workshop on Geothermal Reservoir Engineering, 22 p.

Holmes, R. C., & Huebner, L. (2025). Rethinking power density for geothermal resource estimation. AAPG Bulletin, 109(9), 1147–1159.

Jin, B. (2024). Extrapolation of locations, depths, and flow rates of naturally occurring cold water recharges in the Olkaria Domes geothermal field by integrating numerical simulation and geophysical information. Geothermics, 119, 26 p. https://doi.org/10.1016/j.geothermics.2024.102928

Kamah, M. Y., Dwikorianto, T., Zuhro, A. A., Sunaryo, D., & Hasibuan, A. (2005). The productive feed zones identified based on spinner data and application in the reservoir potential review of Kamojang geothermal area, Indonesia. Proc. World Geothermal Congress, 6 p.

Karakas, O., Dufek, J., Mangan, M. T., Wright, H. M., & Bachmann, O. (2017). Thermal and petrologic constraints on lower crustal melt accumulation under the Salton Sea Geothermal Field. Earth and Planetary Science Letters, 467, 10–17.

Kaspereit, D., Richard, W., Osborn, W. L., Mann, M., & Perez, M. (2016). Field management and expansion potential of the Momotombo geothermal field using numerical simulation and conceptual modeling. Proc. 41st Workshop on Geothermal Reservoir Engineering, 16 p.

Kiryukhin, A. V., Polyakov, A. Y., Usacheva, O. O., & Kiryukhin, P. A. (2018). Thermal-permeability structure and recharge conditions of the Mutnovsky high-temperature geothermal field (Kamchatka, Russia). Journal of Volcanology and Geothermal Research, 356, 36–55.

Kluge, E.-K., Ferguson, C., Reynolds, Z., Motley, C., Libbey, R., Murphy, J., & Akerley, J. (2025). Updated conceptual model and reservoir assessment of the Tuscarora geothermal field: Over a decade of renewable power generation. GRC Transactions, 24 p.

Kondo, K., Itoi, R., Tanaka, T., & Iwasaki, T. (2017). Numerical simulation of the Sumikawa geothermal reservoir, Japan, using iTOUGH2. Proc. 42nd Workshop on Geothermal Reservoir Engineering, 10 p.

Lachassagne, P., Marechal, J. C., & Sanjuan, B. (2009). Hydrogeological model of a high-energy geothermal field (Bouillante area, Guadeloupe, French West Indies). Hydrogeology Journal, 17(7), 1589–1606.

Layman, E. B. (1984). A simple Basin and Range fault model for the Beowawe geothermal system, Nevada. GRC Transactions, 451–456.

Libbey, R., Saputra, I., Murphy, J., Husein, M., Dermawan, F., Archady, D., Webbison, S., Novianto, Deuhart, A., Utomo, D., Johnson, A., Spielman, P., Reynolds, Z., Hadi, J., Cumming, W., Marini, L., Parini, M., Rudyawan, A., Wallis, I., & Kurniawan, I. A. (2026). Conceptual model of the Ijen geothermal field, East Java: Indonesia's first developed blind geothermal system. Proc. World Geothermal Congress, 12 p.

Mackenzie, K. M., Steffen, M. W., Phillips, R., Merz, S. K., Box, P. O., Power, R., Hughes, B., & Parkway, A. (2012). Success of multiple-leg well completions at the San Jacinto-Tizate geothermal field, Nicaragua. New Zealand.

Makovsky, K. A. (2013). The geothermal system near Paisley Oregon: A tectonomagmatic framework for understanding the geothermal resource potential of southeastern Oregon [MSc Thesis].

McLachlan, H. S. (2018). A dissertation submitted in partial fulfillment of the requirements for the degree of Doctor of Philosophy in Geology [PhD Thesis]. University of Nevada Reno.

Mejorada, A., Tolentino, J., & Vicedo, R. (2020). Tiwi Geothermal Field: Reservoir Management After 40 Years of Commercial Operation. Proc. World Geothermal Congress, 8 p.

Melosh, G., Casteel, J., Niggeman, K., & Fairbank, B. (2008). Step-Out Drilling Results at Blue Mountain, Nevada. GRC Transactions, 32, 49–51.

Menzies, A. J., Sanyal, S. K., Granados, E. E., Pham, M., Lima, E., Cuevas, A., & Torres, J. (1996). Analysis of well test data from the high-temperature geothermal system of Amatitlan, Guatemala. GRC Transactions, 20, 821–827.

Menzies, A. J., Co, C. K. D., & Sotunde, O. (2014). Correlation and Modeling of Reservoir Pressure Changes in the Tiwi Geothermal Field, Republic of the Philippines. Proc. Indonesia International Geothermal Convection & Exhibition.

Meixner, J., Schill, E., Grimmer, J. C., Gaucher, E., Kohl, T., & Klingler, P. (2016). Structural control of geothermal reservoirs in extensional tectonic settings: An example from the Upper Rhine Graben. Journal of Structural Geology, 82, 15 p.

Mitchell, M. A., Peacock, J. R., & Burgess, S. D. (2023). Imaging the magmatic plumbing of the Clear Lake Volcanic Field using 3-D gravity inversions. Journal of Volcanology and Geothermal Research, 435.

Moon, H., Melia, K., Aunzo, Z., Siega, F., Pezaro, B., & Lloyd, J. (2022). Mokai reservoir modelling report for reconsenting application 2022 (p. 10 p).

Murphy, J., Holt, R., Morrison, M., & Energy, C. (2017). A Numerical Model Case Study of the Patua Geothermal Field. GRC Transactions, 13 p.

Murphy, J. F., Libbey, R. B., Warren, I., Holt, R. J., Owens, L. B., O'Brien, J., Ltd, S., & Ave, M. (2021). Resource Model Calibration at Neal Hot Springs, Oregon, USA. Proceedings World Geothermal Congress 2020, 6.

Murphy, J.F. and Libbey, R.B. (2026). Reservoir engineering characteristics of geothermal permeability regimes. Proc. 51st Workshop on Geothermal Reservoir Engineering.

Nash, G. D., & Moore, J. N. (2012). Raft River EGS Project: A GIS-Centric Review of Geology. GRC Transactions, 951–958.

Nathenson, M. (1975). Physical factors determining the fraction of stored energy recoverable from hydrothermal convection systems and conduction-dominated areas (No. Open-File Report 75-525; p. 50 p). US Geological Survey.

Nordquist, J., & Delwiche, B. (2013). The McGinness Hills Geothermal Project. GRC Transactions, 57–64.

Orenstein, R., Delwiche, B., & Lovekin, J. (2015). The Don A. Campbell Geothermal Project – Development of a Low-Temperature Resource. Proc. World Geothermal Congress, 6 p.

O'Sullivan, J., Araya, N., Popineau, J., Renaud, T., & Riffault, J. (2023). A natural state and production forecast model of the Salton Sea geothermal field for lithium extraction. GRC Transactions, 47, 241–260.

O'Sullivan, J., Abdurachman, F., Bignall, G., Bromley, C., Dekkers, K., Ghassan, M., Gravatt, M., Hastuti, P., Indra, A., Nugraha, R., Pasaribu, F., Popineau, J., Prasetyo, I., Rai, V., Renaud, T., Riffault, J., Yuniar, D., & O'Sullivan, M. (2023b). A New Modelling Study of the Kamojang Geothermal Field. Proc. 48th Workshop of Geothermal Reservoir Engineering, 13 p.

Parini, M., & Riedel, K. (2000). Combining probabilistic volumetric and numerical simulation approaches to improve estimates of geothermal resource capacity. Proc. World Geothermal Congress, 2785–2790.

Pester, S., Agemar, T., Alten, J.-A., Kuder, J., Kuehne, K., Maul, A.-A., & Schulz, R. (2010). GeotIS – the Geothermal Information System for Germany. 6 p.

Pineda, J. A. G., Chavez, G., Osorno, A., Lawless, J. V., Ussher, G. N., Mackenzie, K. M., Malate, R. C. M., Lovelock, B. G., & Prestage, A. E. (2020). The Conceptual Model and Its Evolution Over 15 Years of Development and Operation: San Jacinto-Tizate Geothermal Field, Nicaragua. Proc. World Geothermal Congress, 13 p.

Pollack, A., Cladouhos, T. T., Swyer, M., Horne, R., & Mukerji, T. (2020). Stochastic structural modeling of a geothermal field: Patua geothermal field case study. Proc. 45th Workshop on Geothermal Reservoir Engineering, 20 p.

Porras, E. A., & Itoi, R. (2006). The Momotombo geothermal system and its conceptual model. GRC Transactions, 33–38.

Porras, E. A., Tanaka, T., Fujii, H., & Itoi, R. (2007). Numerical modeling of the Momotombo geothermal system, Nicaragua. Geothermics, 36(4), 304–329.

Porras, E. A., & Bjornsson, G. (2010). The Momotombo Reservoir Performance upon 27 Years of Exploitation. Proc. World Geothermal Congress, 5 p.

Porras, E., & Xicara, J. (2020). A new numerical model of Amatitlan geothermal system, Guatemala. Proc. World Geothermal Congress, 12 p.

Potter, J., Misal, A., & Azwar, L. (2020). Chloride Model of Ngatamariki Geothermal System. Proc. 45th Workshop on Geothermal Reservoir Engineering, 11 p.

Ramirez, G., Zuza, R., Johnson, A., Murphy, J., & Akerley, J. (2023). Integrated conceptual model of sedimentary basin-hosted geothermal fields in Imperial Valley, CA. 1551–1572.

Renaud, T., Croucher, A., Dekkers, K., Gravatt, M., O'Sullivan, M., Popineau, J., Riffault, J., Tonkin, R., & O'Sullivan, J. (2025). Updated modelling of the Salton Sea geothermal field. Proc. 50th Workshop on Geothermal Reservoir Engineering, 12 p.

Rop, E. (2013). Interpretation of recent temperature and pressure data and updated conceptual model of the Greater Olkaria Geothermal System, Kenya. United Nations Geothermal Training Programme, 32, 769–806.

Rowland, J. V., & Simmons, S. F. (2012). Hydrologic, magmatic, and tectonic controls on hydrothermal flow, Taupo volcanic zone, New Zealand: Implications for the formation of epithermal vein deposits. Economic Geology, 107(3), 427–457.

Rowley, P. D., Rutledge, E. F., Maxwell, D. J., Dixon, G. L., & Wallace, C. A. (2013). Geology of the Sulphurdale geothermal-resource area, Beaver and Millard counties, Utah (Open-File Report No. 609; p. 33 p).

Sambrano, B. G., Aragon, G. M., & Nogara, J. B. (2010). Quantification of injection fluids effects to Mindanao geothermal production field productivity through a series of tracer tests, Philippines. Proc. World Geothermal Congress, 13 p.

Sanyal, S. K., & Butler, S. J. (2005). An Analysis of Power Generation Prospects from Enhanced Geothermal Systems. Proc. World Geothermal Congress, 6 p.

Siler, D. L., Faulds, J. E., Hinz, N. H., & Queen, J. H. (2021). Three-dimensional geologic map of the Brady geothermal area, Nevada (Scientific Investigations Map, pp. 1–20) [Scientific Investigations Map 3469].

Siler, D. L. (2023). Structural discontinuities and their control on hydrothermal systems in the Great Basin, USA. Geoenergy, 1(1), 10 p.

Sims, D. B., Neuhoff, P. S., & Norton, D. L. (2025). Structural, mineralogical, and geophysical data implications for the development of the Salton Sea magma-hydrothermal system. Proc. 50th Workshop on Geothermal Reservoir Engineering, 18 p.

Smith, T., Sonnenthal, E., Nakata, N., Cladouhos, T., Swyer, M., Energy, C., & Energy, C. (2023). A thermal, hydrological and mechanical model of Patua geothermal field, Nevada. Proc. 48th Workshop on Geothermal Reservoir Engineering, 9 p.

Stimac, J., Nordquist, G., Suminar, A., & Sirad-Azwar, L. (2008). An overview of the Awibengkok geothermal system, Indonesia. Geothermics, 37(3), 300–331.

Stober, I., Fritzer, T., Obst, K., Agemar, T., & Schulz, R. (2017). Deep geothermal energy: Principles and application possibilities in Germany (Second revised English edition, as at January 2017). Leibniz Institute for Applied Geophysics.

Suryadarma, Dwikorianto, T., Zuhro, A. A., & Yani, A. (2010). Sustainable development of the Kamojang geothermal field. Geothermics, 39(4), 391–399.

Vidal, J., & Genter, A. (2018). Overview of naturally permeable fractured reservoirs in the central and southern Upper Rhine Graben: Insights from geothermal wells. Geothermics, 74, 57–73.

Wallis, I., Moon, H., Clearwater, J., Azwar, L., & Barnes, M. (2015). Perspectives on geothermal permeability. Proceedings 37th New Zealand Geothermal Workshop, 7 p.

Wallis, I. C., Rowland, J. V., Cumming, W., & Dempsey, D. (2017). The subsurface geometry of a natural geothermal reservoir. Proc. 39th New Zealand Geothermal Workshop, 9 p.

Wilmarth, M., & Stimac, J. (2015). Power density in geothermal fields. Proc. World Geothermal Congress, 7 p.

Wilmarth, M., Stimac, J., & Ganefianto, G. (2020). Power density in geothermal fields, 2020 update. Proc. World Geothermal Congress, 8 p.

Wiggins, A., Silva, N., Johnson, A., Reynolds, Z., Libbey, R., & Murphy, J. (2025). Successful Injection Well 85A-18 at the Beowawe Geothermal Field, Nevada, USA: Implications of High Permeability from Injection Testing. GRC Transactions, 1639–1659.

White, D. E. (1968). Hydrology, activity, and heat flow of the Steamboat Springs thermal system, Washoe County, Nevada (No. Geological Survey Professional Paper 458-C). USGS.

Zuhro, A. A. (2004). Numerical modelling of the Kamojang geothermal system, Indonesia. United Nations Geothermal Training Programme, 475–492.